ELSEVIER

Applied Numerical Mathematics 27 (1998) 83–108

APPLIED NUMERICAL MATHEMATICS

A numerical model of a high performance two-stroke engine

J. van Leersum

Ian Williams Tuning, P.O. Box 633, Plympton, South Australia, 5038, Australia

Abstract

A numerical model of the main processes occurring in a two-stroke internal combustion engine is described. This model does not have many of the restrictions of previous models in the literature. Particular attention is given to modelling the duct flows using a flux conservative Lax–Wendroff type algorithm modified by the use of flux splitting and flux limiters. This makes the model well able to cope with very high specific power output engines. Numerical, convergence, and flux conservation properties of the model are illustrated and engine performances predicted by it are shown to compare well with experimental data from a high performance 125cc engine and a medium performance 100cc engine. © 1998 Published by IMACS/Elsevier Science B.V.

1. Introduction

This study describes a model of the fluid flow through a two-stroke, spark ignition internal combustion engine, a schematic diagram of which is shown in Fig. 1. The salient features of this engine's operation are:

- The fresh charge fires near the top of the piston's stroke, forcing the piston to descend. This is the combustion phase.
- When the top of the piston dips below the top of the exhaust port, gas from the cylinder box begins to flow into the exhaust duct.
- As the piston descends further, it compresses a fresh charge in the crankcase, which begins to flow into the transfer duct, and from there into the cylinder box once the piston descends far enough to open the transfer port in this box.
- The fresh charge entering the cylinder assists any favorable pressure gradient across the exhaust port in forcing the spent exhaust gases into the exhaust duct. Simultaneously, the cylinder is charged with a fresh mixture. This process is known as scavenging.
- While the piston is ascending, it creates a low pressure in the crankcase box, and when the bottom edge of the piston uncovers the inlet port, a fresh charge of fuel/air is drawn into this box.
- The piston rises, eventually closing both the exhaust and transfer ports so that the last part of the compression and the combustion takes place in a completely closed space.

PII S0168-9274(97)00108-6

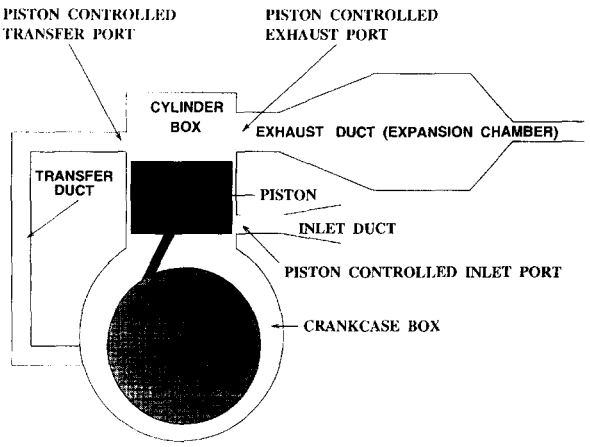

Fig. 1. Schematic of two-stroke engine.

Clearly, the amounts of gas flowing into and out of the two boxes are very dependent upon the gas dynamics in the inlet, transfer and exhaust ducts.

The capability of a numerical model to predict accurately the performance of a high specific power output two-stroke internal combustion engine is very dependent upon the way in which duct flows (particularly, the exhaust duct flow) within the engine are modelled. The reason for this is that most engines of this type rely on pressure waves in the exhaust ducts to ensure that the cylinder is emptied of its exhaust gas and is filled with a large amount of fresh charge as efficiently as possible. Ideally then, a low pressure wave is required to arrive at the exhaust port just after it opens, to suck out the burnt gas, and a high pressure wave is required at that port some time before the exhaust port closes to stop part of the fresh charge escaping into the exhaust duct. It is crucial, therefore, to model these pressure waves accurately, because, as Blair [3] has noted, the wrong exhaust duct can cut an engine's output by 50%.

Traditionally, many authors, for example Blair [3], Annand and Roe [1], and Benson et al. [2] have modelled duct flows using the mathematical method of characteristics. These methods fall into two categories:

- Isentropic models, where the flow is assumed to be isentropic everywhere in the duct.
- Non-isentropic models, where friction, heat transfer, and change of reference temperature within the duct are all considered.

Isentropic models suffer from the limitation that a reference temperature for each duct is required as an input. The model then relates each duct temperature to its chosen reference temperature. Clearly, if the wrong reference temperature is specified, the wave speeds are in error, as are the model predictions. Whilst Blair [3] gives some guidance on choosing reference temperatures for different types of engine, the correct temperature is hard to predict for an "unknown" engine. Nevertheless, when this parameter is chosen correctly, model predictions of engine output can be very good.

Non-isentropic models which use the method of characteristics do not suffer from the above restriction. However, the method of characteristics generally has the following limitations:

- Difficulties in modelling shock waves, contact discontinuities and transonic flow without complicated "add-ons". Such phenomena occur in high performance engines.

- A need to "seed" the computational field with a large number of *path-lines* so that changes in temperature can be modelled correctly.
- Numerical smearing caused by the need to interpolate characteristic positions between nodes, when the "mesh" method of characteristics (Benson et al. [2]) is used. The natural method of characteristics (Benson et al. [2]) causes problems with mesh points being non-uniformly distributed in both the space and time domains and is used infrequently for this reason.

The main problem with traditional numerical methods which are non-characteristic based (e.g., the standard Lax–Wendroff family of methods (Press et al. [18])) has been their inability to model the consequences of step changes in duct end temperatures and pressures which occur as a result of ports opening and closing. Since the early 1970s, a class of numerical methods has become available which overcomes this inherent difficulty. This is the Total Variation Diminishing (TVD) class, so called because of its ability to contain the unstable oscillations produced by traditional methods. An excellent review of these and related methods is contained in Yang and Przekwas [25]. Winterbone and Pearson [24] used one such method for modelling flow in an engine duct, but their study was limited to a duct with constant cross-section area, and addressed flow resulting from a step change in inlet conditions at one end (the de Haller test). Whilst results were good, the present author found that methods which were satisfactory for this problem produced unacceptable oscillations when used for ducts with a cross-section area variation of the type found in two-stroke expansion chambers, driven by real engine cylinder temperature and pressure variations. More recently, Neumeyer et al. [16] and Chiou et al. [7] have used such methods to model what appear to be low specific power output engines. Both of these studies were restricted by some or all of the following assumptions:

- The fluid obeyed perfect gas laws and the internal energy equation used was based on perfect gas relationships.
- No account was taken of the changing composition of the gas as it progressed through the engine from a fresh charge to a partially burnt gas.
- Isentropic flow equations applied at all duct boundaries, regardless of flow direction.
- The "perfect mixing" assumption was made in the scavenging model.

Corberan et al. [9] appear to have produced a comprehensive model of a high specific power output two-stroke engine, based on TVD numerical methods used to model duct flows, and a comprehensive scavenging model. There is not enough detail given in their paper to allow a reader to reproduce the results obtained. However, the model does appear to be restricted by the use of perfect gas relationships for fluid internal energy as a function of temperature.

In this study, none of the above assumptions is made and the TVD-like numerical method used to model duct flows is based on a completely different algorithm from that used in any of the studies mentioned above.

2. Mathematical and numerical models

The following subsections describe models for each of the main processes which occur in a two-stroke engine. The study is restricted to single cylinder engines, containing ducts in which cross-section areas vary slowly in the axial direction. It is assumed that all velocities other than axial ones are negligible.

2.1. Gas properties

The perfect gas equation

$$P = \rho RT \tag{1}$$

is assumed throughout the study. However, an invertible relation between the internal energy E, temperature T and gas purity w is required for the duct flow and boundary condition models. The simple perfect gas based relationship is inadequate over the 250–3000K operating temperature range of an engine (Winterbone and Pearson [24]), and a quadratic fit for E as a function of T is little better.

Rational polynomials were fitted to appropriate data at 5K intervals from Keenan and Kaye [15] (for air), and Blair [3] (for exhaust gas) to produce a usable relationship between gas internal energy, temperature, and purity. The nonlinear least squares minimization technique due to Nelder and Meade, described in Press et al. [18] was used to carry this out. Fits with errors of less that 0.5% were obtained with both a quadratic numerator and denominator as follows:

$$E = \frac{\mu_0 + \mu_1 T + \mu_2 T^2}{\mu_3 + \mu_4 T + T^2} \tag{2}$$

with

$$\begin{aligned}
\mu_0 &= 4.1780473 \times 10^{10} - 2.5514749 \times 10^9 w,\\
\mu_1 &= 9.7194612 \times 10^{10} - 6.8103807 \times 10^9 w,\\
\mu_2 &= 4.2923950 \times 10^7 - 8.7154810 \times 10^6 w,\\
\mu_3 &= 1.3956866 \times 10^8,\\
\mu_4 &= 2.2950588 \times 10^4.
\end{aligned}$$

This procedure allowed the required inversion of the function for T by solving a quadratic equation given E and w.

Another variable required for the duct flow and boundary condition models is γ, the ratio of specific heats. This can be calculated by noting that

$$\gamma = \frac{c_p}{c_v} = 1 + \frac{R}{c_v}$$

and since

$$c_v = \left(\frac{\partial E}{\partial T}\right)_v,$$

Eq. (2) can be used to calculate the partial derivative, and hence c_v and γ.

2.2. Duct flow model

The equations describing conservation of heat, momentum, and internal energy of quasi one-dimensional compressible flow in a duct of varying cross-section area are known as the Euler equations. They can be written (Corberan et al. [9])

$$\frac{\partial}{\partial\theta}\begin{bmatrix}\rho A\\ \rho UA\\ \rho E_0 A\end{bmatrix}+\frac{\partial}{\partial x}\begin{bmatrix}\rho UA\\ (\rho U^2+P)A\\ \rho U\left(E_0+\dfrac{P}{\rho}\right)A\end{bmatrix}=\begin{bmatrix}0\\ P\dfrac{\partial A}{\partial x}-\rho AG\\ \rho A\dot{q}\end{bmatrix}, \tag{3}$$

where

$$G=\frac{4fU|U|}{2D}$$

and

$$\dot{q}=\frac{2f}{D}\frac{\gamma}{\gamma-1}R|U|(T_{\text{wall}}-T_{\text{stag}}) \tag{4}$$

from the Reynolds analogy (Poloni et al. [17]). T_{stag} is the gas stagnation temperature, which can be calculated from the gas temperature and velocity, whilst T_{wall} can be eliminated by using the Reynolds analogy outside the duct if the external duct heat transfer coefficient and ambient air temperature are known.

The numerical method chosen to solve these equations inside the ducts is called flux splitting. It follows closely the scheme outlined by Grossman and Walters [11] which invokes a flux splitting due to Steger and Warming [21]. Its advantage lies in the fact that it is capable of selecting a physically admissible solution (Yang and Przekwas [25]), hence its use in this study.

Denoting

$$\xi=\rho U \quad \text{and} \quad \zeta=\rho E_0$$

the flux terms in Eq. (4) can be written

$$\begin{bmatrix}F_\rho\\ F_\xi\\ F_\zeta\end{bmatrix}=\begin{bmatrix}\xi\\ \dfrac{\xi^2}{\rho}+P\\ \dfrac{\xi}{\rho}(\zeta+P)\end{bmatrix}=\tilde{Z}\begin{bmatrix}\rho\\ \xi\\ \zeta\end{bmatrix}, \tag{5}$$

where the common area multiplier A has been cancelled out for the purposes of the following discussion. The last equality in this equation shows the form that the flux vector must take to allow a flux splitting to be carried out. The matrix $\tilde{Z}$ must therefore be found.

It is easy to verify that

$$\tilde{Z}=\begin{bmatrix}0 & 1 & 0\\ \dfrac{(\tilde{\gamma}-3)U^2}{2} & (3-\tilde{\gamma})U & (\tilde{\gamma}-1)\\ -\tilde{\gamma}UE+\dfrac{(\tilde{\gamma}-2)U^3}{2} & \tilde{\gamma}E+\dfrac{(3-2\tilde{\gamma})U^2}{2} & \tilde{\gamma}U\end{bmatrix} \tag{6}$$

satisfies this relationship.

This is actually the Jacobian transformation, assuming a perfect gas relationship for the internal energy, with one important difference. The variable $\tilde{\gamma}$ is not the ratio of specific heats. It is a variable calculated at each point which ensures that the relationship

$$P = (\tilde{\gamma} - 1)\rho E \tag{7}$$

always holds. When $\tilde{\gamma}$ is required, it is computed from the known dependent variables ρ and P. The latter variable is computed from Eq. (1), with T resulting from the inversion of Eq. (2). E is found from the relationship

$$\rho E = \rho E_0 - \rho\frac{U^2}{2} = \zeta - \frac{\xi^2}{2\rho}. \tag{8}$$

2.2.1. Flux splitting

The mechanics of flux splitting is discussed in Hoffman [14]. The matrix of eigenvalues corresponding to $\tilde{Z}$ can be written

$$\tilde{\Lambda} = \tilde{S}^{-1}\tilde{Z}\tilde{S}, \tag{9}$$

where it can be shown that

$$\tilde{\Lambda} = \begin{pmatrix} U & 0 & 0 \\ 0 & U + \tilde{a} & 0 \\ 0 & 0 & U - \tilde{a} \end{pmatrix}.$$

In this relationship,

$$\tilde{a}^2 = \tilde{\gamma}P/\rho. \tag{10}$$

$\tilde{a}$ is not the local speed of sound, but an analogous quantity based on $\tilde{\gamma}$. The columns of the matrix $\tilde{S}$ are the right eigenvectors of $\tilde{Z}$ which can be written

$$\tilde{S} = \begin{pmatrix} 1 & 1 & 1 \\ U & U + \tilde{a} & U - \tilde{a} \\ \frac{1}{2}U^2 & \tilde{B} + U\tilde{a} & \tilde{B} - U\tilde{a} \end{pmatrix}, \tag{11}$$

where

$$\tilde{B} = \frac{\tilde{a}^2}{\tilde{\gamma} - 1} + \frac{U^2}{2}.$$

From Eq. (9),

$$\tilde{Z} = \tilde{S}\tilde{\Lambda}\tilde{S}^{-1}.$$

Flux splitting involves breaking the eigenvalue matrix $\tilde{\Lambda}$ into one matrix containing only positive eigenvalues, and another containing only negative eigenvalues. This allows the matrix $\tilde{Z}$ to be written as

$$\tilde{Z} = \tilde{Z}^+ + \tilde{Z}^-,$$

where the "+" and "−" superscripts refer to the parts of $\widetilde{Z}$ obtained using the positive and negative parts of $\widetilde{\Lambda}$, respectively. Eq. (5) can then be used to break the flux vector into one part attributable to the positive eigenvalues of $\widetilde{\Lambda}$ and another attributable to the negative eigenvalues of $\widetilde{\Lambda}$. Grossman and Walters [11] show these components to be

$$\begin{pmatrix} F_\rho^\pm \\ F_\xi^\pm \\ F_\zeta^\pm \end{pmatrix} = \begin{pmatrix} \dfrac{\rho}{2\widetilde{\gamma}}\left[2(\widetilde{\gamma}-1)\lambda_1^\pm + \lambda_2^\pm + \lambda_3^\pm\right] \\ UF_\rho^\pm + \dfrac{\rho\widetilde{a}}{2\widetilde{\gamma}}\left(\lambda_2^\pm - \lambda_3^\pm\right) \\ \dfrac{U^2}{2}F_\rho^\pm + \dfrac{\rho}{2\widetilde{\gamma}}\left[U\widetilde{a}\left(\lambda_2^\pm - \lambda_3^\pm\right) + \dfrac{\widetilde{a}^2}{\gamma-1}\left(\lambda_2^\pm + \lambda_3^\pm\right)\right] \end{pmatrix}, \tag{12}$$

where

$$\lambda_1 = U, \qquad \lambda_2 = U + \widetilde{a}, \qquad \lambda_3 = U - \widetilde{a}$$

and

$$\lambda_i^\pm = \tfrac{1}{2}\left(\lambda_i \pm |\lambda_i|\right) \quad \text{for } i = 1, 2, 3.$$

The spatial derivatives of fluxes are then computed using upwind discretization, relative to the signal propagation speeds. This flux splitting is based on $\widetilde{\gamma}$ and was first proposed by Steger and Warming [21]. As it proved satisfactory for this study, no other form of flux splitting was investigated.

2.2.2. Equation discretization

A two step Lax–Wendroff type algorithm, second order almost everywhere in both space and time (Grossman and Walters [11]) was used to discretize the set of equations (3). Control volume averaging over each cell was a minor modification made to the algorithm as presented in [11]. Denoting Q to represent either ρ, ξ or ζ, the algorithm is as follows.

Let

$$QQ_1 = A_{i+1/2}F^+\left(Q^-_{i+1/2}\right) - A_{i-1/2}F^+\left(Q^-_{i-1/2}\right)$$

and

$$QQ_2 = A_{i+1/2}F^-\left(Q^+_{i+1/2}\right) - A_{i-1/2}F^-\left(Q^+_{i-1/2}\right),$$

where Q has been written as a bracketed argument of F instead of as a subscript, for readability and ease of notation.

The first step of the algorithm is

$$\overline{Q}_i = Q_i^n - \delta\theta\frac{QQ_1 + QQ_2}{v_i} + \delta\theta Q^n_{i_{\text{non-homogeneous}}},$$

where the last term is the volume averaged appropriate friction or heat transfer term in Eq. (3) evaluated at the initial state Q_i^n then divided by v_i, the volume of cell i. The second step can then be written

$$QQ_1 = A_{i+1/2}F^+\left(\overline{Q}^-_{i+1/2}\right) - A_{i-1/2}F^+\left(\overline{Q}^-_{i-1/2}\right)$$

and

$$QQ_2 = A_{i+1/2}F^-\left(\overline{Q}^+_{i+1/2}\right) - A_{i-1/2}F^-\left(\overline{Q}^+_{i-1/2}\right)$$

leading to

$$Q_i^{n+1} = \tfrac{1}{2}\left(Q_i^n + \overline{Q}_i - \delta\theta \frac{(QQ_1 + QQ_2)}{v_i} + \delta\theta \overline{Q}_{i_{\text{non-homogeneous}}} \right),$$

where the last term is the appropriate friction or heat transfer term in Eq. (3) evaluated at the intermediate state, $\overline{Q}_i$, then divided by v_i.

The non-homogeneous terms on the right hand side of the momentum equation in the set of equations (3) contain the term

$$\int_{i-1/2}^{i+1/2} P \frac{\partial A}{\partial x}\, \mathrm{d}x = \int_{i-1/2}^{i+1/2} P\, \mathrm{d}A.$$

In the flux limiting process (Section 2.2.3), linear interpolation of pressure over each cell is established. If δP is the difference in pressure between the boundaries of cell i, then the above expression can be integrated by parts to yield

$$P_i(A_{i+1/2} - A_{i-1/2}) + \delta P \left(\frac{A_{i+1/2} + A_{i-1/2}}{2} - \frac{v_i}{\delta x} \right).$$

Clearly, all geometry related quantities need to be evaluated only at the start of each simulation.

The superscripts $\pm$ on the flux functions, F, indicate that they should be evaluated as in Eq. (12). Grossman and Walters [11] recommended evaluating the dependent variables at the half node points using the extrapolations

$$Q^-_{i+1/2} = Q_i + \tfrac{1}{2}(Q_i - Q_{i-1}) \quad \text{and} \quad Q^+_{i+1/2} = Q_{i+1} + \tfrac{1}{2}(Q_{i+1} - Q_{i+2}).$$

This procedure failed when integrated into the duct flow model. It produced negative values of density because of the non-limiting nature of the extrapolation. It was therefore necessary to apply a flux limiter to the calculation of some variables at the half node points, and hence the corresponding fluxes.

2.2.3. *Flux limiters*

Yang an Przekwas [25] have surveyed a number of different flux limiters proposed for solving systems of hyperbolic conservation laws. The one which proved most successful in the numerical scheme of Section 2.2.2 was similar to that of Davis [10], which in turn is very similar to the original van Leer [22] MUSCL limiter. This limiter considers the variable in question at the points $i-1$, i and $i+1$, deriving a linear relationship for the spatial variation of the variable in the interval $(i-1/2,\ i+1/2)$ as follows.

Let

$$\Delta_{i+1/2} = Q_{i+1} - Q_i \quad \text{and} \quad \Delta_{i-1/2} = Q_i - Q_{i-1}.$$

Set

$$S_m = \min\left(\tfrac{1}{2}|\Delta_{i+1/2} + \Delta_{i-1/2}|, 2l|\Delta_{i-1/2}|, 2l|\Delta_{i+1/2}|\right) \quad \text{with } 0.5 \leqslant l \leqslant 1$$

and

$$S = \begin{cases} \operatorname{sign}(\Delta_{i+1/2} + \Delta_{i-1/2}) S_m, & \text{if } \Delta_{i+1/2}\Delta_{i-1/2} > 0, \\ 0, & \text{otherwise.} \end{cases}$$

Then

$$Q_{i+x} = Q_i + xS, \quad |x| < \tfrac{1}{2},$$

thus establishing an interpolation over each cell for calculating the variables at the node half-points:

$$Q^-_{i+1/2} = Q_i + \tfrac{1}{2} S, \tag{13}$$

$$Q^+_{i-1/2} = Q_i - \tfrac{1}{2} S. \tag{14}$$

This interpolation produces a continuous variation in each of the properties chosen between $i - 1/2$ and $i + 1/2$, allowing for possible discontinuities in the properties at the boundaries of this interval. Provided that the recommendations of Grossman and Walters [11] are followed in regard to using density, momentum and *pressure* (instead of internal energy E) for the interpolation variables, the above scheme proved satisfactory for solving the flow equations at all interior points in the duct.

2.2.4. *Purity calculation*

The previous sections have described the modelling of compressible flow of a gas in a duct. The purity of the cylinder gas in a two-stroke engine varies between close to zero during the exhaust phase, and sometimes nearly one when the exhaust port closes. The purity at exhaust port closure determines how much cylinder charge is available for combustion, which, in turn determines the engine power output. Gas purity must therefore be calculated at each mesh point in each duct at the end of each time step, as well as in each "box".

A similar conservation equation to Eq. (3) can be written for the pure (air) component of the gas:

$$\frac{\partial(\rho w A)}{\partial \theta} + \frac{\partial(\rho w U A)}{\partial x} = 0. \tag{15}$$

The two step discretization described in Section 2.2.2 can be used for this equation. Given that the gas purity at each node is known at the beginning of each time step, the fluxes of ρw on the cell boundaries can be computed as follows.

On the right boundary of the cell with node number i, the total mass flux is

$$F^+\left(\rho^-_{i+1/2}\right) + F^-\left(\rho^+_{i+1/2}\right).$$

If this is possitive, the flux of ρw is calculated by multiplying it by w_i. If negative, this flux is calculated by multiplying it by w_{i+1}. This avoids interpolating w as described in Section 2.2.3.

Once the fluxes of ρw are computed, the numerical scheme described in Section 2.2.2 can be used to compute a provisional value of ρw at the end of the time step at node i. Since ρ can be calculated separately, w can then be found. The final values of ρw and w at node i can be found by applying the second step of the algorithm.

2.2.5. *Numerical stability*

The above explicit algorithm is stable only for Courant numbers less than unity. The speed to use in this Courant number calculation is

$$\mathrm{Max}\left(|U \pm \tilde{a}|\right).$$

Time steps were chosen dynamically by using the maximum (in modulus) wave velocity at each mesh point in each duct, and the maximum Courant number chosen for the particular simulation, to

calculate a maximum allowable time step at each node. The time step used was the minimum of all these, ensuring stability at all nodes.

Mean temperatures in the engine inlet and transfer ducts (Fig. 1) are typically 60°C whereas those in the exhaust duct are typically 600°C. Numerical experiments suggested that to ensure that the time steps were not constrained severely by any one duct, the spatial discretization for the cooler ducts should be about half that of the exhaust duct.

2.3. Boundary conditions

As noted in Hoffman [14], boundary conditions are best expressed in terms of Riemann variables, using the method of characteristics. There are two parts to describing these boundary conditions: a flow model, which describes flow between a duct and an adjacent box, and a compatibility model which allows calculation of the "incident" box Riemann variable and local reference speed of sound.

2.3.1. The flow model

The flow model needs to take account of the flow direction and whether or not the flow in the constriction or port between the box and the duct is subsonic or sonic. The models used in this study are modifications of those described by Blair [4]. The latter are extensions of those presented by Wallace and Nassif [23] and incorporate many of the ideas in Blair and Cahoon [5]. In line with these studies, it is assumed that the gas in each box is stagnant. The region between the stagnant air in the box and the entrance to the adjacent duct is assumed to take the form of a convergent–divergent nozzle, having one end in the box and the other end at the duct entrance. Typical time intervals in a simulation correspond to less than one degree of crankshaft revolution, and over this time scale, a steady flow in the nozzle is assumed. The cross-section area of the constriction in the nozzle is assumed to be equal to the physical engine port area multiplied by a discharge coefficient. All port areas are determined from the engine geometry and the relationship between the piston position and the angular displacement of the crankshaft. Discharge coefficients are functions of port area, flow direction, and pressure ratio across the port. They have been measured by Blair et al. [6] under a variety of situations. Average values from this reference have been used in this study.

For gas flow out of a box, the flow between the box and the nozzle constriction is assumed to be isentropic. However, for flow between the constriction and the nozzle exit the isentropic assumption is replaced by the steady flow momentum conservation equation when the flow at the nozzle constriction is sub-sonic. The momentum equation is replaced by the assumption of sonic velocity at the vena-contracta when the flow is sonic. Wallace and Nassif [23] argued strongly that this was the correct assumption to make.

For gas flow into a box, it is assumed that the flow is isentropic. When the flow is subsonic, it is assumed that the pressure at the nozzle exit is equal to the box pressure. This assumption is replaced by the assumption of sonic velocity at the nozzle constriction when the flow is sonic.

The equations resulting from the models described above are solved using the Newton–Raphson technique. The inputs to these equations are the nozzle constriction area, the box temperature and pressure, and the value of the "incident" Riemann variable, at the duct end. Calculation of this last parameter is discussed below. The output is the value of the reflected Riemann variable, and, in the case of outflow, the reference speed of sound at the duct end in question.

The equations are notorious for generating spurious roots and are solved over the entire solution space at the beginning of each simulation. This allows strict controls and checks to be made on the solutions as they are generated sequentially. They are stored in a look-up table and a multi-dimensional linear interpolation is used to access them during the simulation.

2.3.2. The compatibility relations

When the non-homentropic mesh based numerical method of characteristics (Hoffman [14]) is applied at an interior duct node, the solution of the compatibility equations for each of the Riemann variables and the path line enable computation of the required dependent variables at the end of a time step. Since there is no duct section beyond the end node, one of the compatibility equations at this node disappears. For outflow from a box, gas flows into the duct, and there is no path line compatibility equation. However, as described above, the port flow equations provide two relationships involving the pressure and temperature in the adjacent box, the effective nozzle constriction area, the incident and reflected Riemann variables at the duct end node and the reference speed of sound at that node. There are therefore still three equations which can be solved for these last three variables, assuming that the box variables are known. For inflow to the box, the flow equations do not provide a relationship for the reference speed of sound, but the compatibility equation for this variable can be written since the path line is now contained within the duct interior. There are therefore enough equations to calculate all of the duct end variables in this case too.

The mesh based method of characteristics requires that the state variables be continuous so that they may be interpolated on each cell over which the algorithm is applied. In the duct flow model of Section 2.2, discontinuities in the relevant variables are allowed only on cell boundaries, these being half node points. The duct was therefore discretized with grid points starting and ending half a mesh length in from each duct end so that the Riemann variables at the duct ends were calculated on cell boundaries. The piecewise linear interpolation for the variables ρ, ζ and P resulting from the flux limiting process (Section 2.2.3) provided the required interpolation for application of the method of characteristics in the duct end cells.

In order to construct the piecewise interpolation for cells adjacent to boxes, fluid states one half of a mesh length outside the duct end were required. After considerable experimentation this fluid state was assumed to be the same as that at the duct end. This state is available at the beginning of the time step since it is the state already computed by the method of characteristics at the end of the previous time step. The rationale for this choice was that having the same state outside the duct end would not affect fluid states in the duct. This procedure proved very stable and gave excellent results.

The dependent variables at the end of the duct were used to calculate the fluxes at these ends. Because the duct ends are cell boundaries, these fluxes were used directly in the duct flow model described in Section 2.2.

2.3.3. Boundary state calculation procedure

For a given box pressure and temperature, the procedure for calculating the dependent variables at the duct ends was iterative. This is because the numerical implementation of the method of characteristics was of the predictor corrector type (Hoffman [14]) and the associated equations needed to be solved in conjunction with the look-up table generated by the flow model. At the beginning of a time step,

the adjacent box pressure and temperature at the end of the time step are unknown. The procedure adopted for calculating both these and the duct end variables was to:

1. Use linear extrapolation over the previous time step to estimate starting values of the box variables and the duct end variables at the end of the current time step.
2. Keep the box pressure and temperature fixed and iterate as described in the preceding sections to estimate a consistent set of duct end variables at the end of the time step. Use these to calculate fluxes of mass and energy for the box state prediction model. A combination of successive substitution and Aitken acceleration proved to be a very efficient method for carrying this out.
3. Use the mass and energy fluxes from step 2 in the box state prediction model (Section 2.4) to predict new estimates of box pressure and temperature.
4. Iterate steps 2 and 3 until relative differences between successive box variables change by less than 10^{-5}.

2.4. Gas states in boxes

Three distinct models were used to describe box gas states:

- open boxes which have at least one port open,
- closed boxes in which combustion occurs,
- closed boxes where no combustion occurs.

In each case the box volume may be fixed (e.g., box silencer) or it may vary (e.g., cylinder). A variable volume box has its volume controlled by a piston, a geometric relationship between crankshaft angle and piston position allowing calculation of the volume at any instant.

2.4.1. Open boxes

A box is open if at least one of its ports is open. The model for calculating the change in box state over a time interval is essentially the same as that used by many engine modellers, for example, Blair [3]. It assumes that the box has a uniform thermodynamic state at any particular instant and that the heat lost through the box walls in the process is negligible compared with internal energy, work and enthalpy changes over each time interval.

Conservation of mass in a box over the time interval $(j, j+1)$ leads to the equation

$$M^{j+1} = M^j + m^{\text{in}} - m^{\text{out}}, \tag{16}$$

where m^{in} and m^{out} are the mass flows into and out of the box over the time interval. Likewise, conservation of internal energy in a box over the same time interval leads to the equation

$$(ME)^{j+1} = (ME)^j - \left[(mH)^{\text{out}} - (mH)^{\text{in}}\right] - \tfrac{1}{2}\left(P^{j+1} + P^j\right)\left(V^{j+1} - V^j\right), \tag{17}$$

where E is the specific internal energy of the fluid in the box, H^{in} and H^{out} are the specific *total* enthalpies flowing into and out of the box during the time interval, and the last term is the work done over the time interval.

At the beginning of the time interval the box temperature, pressure and volume are all known, hence the corresponding gas mass and enthalpy can be calculated.

The boundary condition model (Section 2.3) allows calculation of all gas states, mass fluxes and enthalpy fluxes at duct ends. By using the trapezoidal numerical integration rule, each enthalpy related term in Eq. (17) can be estimated by averaging the products of duct end mass flow rate and specific

enthalpy at the beginning and end of a time interval and multiplying the result by the time interval. As described in Section 2.3, the solution of Eqs. (16) and (17) needs to be carried out iteratively with the boundary condition equations. This is because the enthalpies and flow rates of the gas flowing into and out of the box are dependent on appropriate duct end states, which are in turn dependent upon box pressure and temperature. Since $E = E(T)$ (Section 2.1) and from the perfect gas relationship $P = P(T, V)$, Eqs. (16) and (17) can be solved implicitly for T at each iteration of the algorithm.

It is assumed that the purity in the crankcase is uniform, hence the following equation can be used to calculate the box purity (W^{j+1}) at the end of each time step:

$$(MW)^{j+1} = (MW)^j + m^{\text{in}} w^{\text{in}} - m^{\text{out}} W^j, \tag{18}$$

where it is assumed, to avoid an iterative process, that w^{in} is evaluated at the end node of the duct providing inflow at the start of the time interval.

2.4.2. Scavenging

The scavenging model adopted is the two zone model similar to the one described in Blair [3]. Here, the fresh charge entering the cylinder is distributed in user supplied percentages to three locations:

- a cylinder zone containing only fresh charge (the perfect displacement zone),
- a cylinder zone containing only fully mixed gas (the perfect mixing zone),
- the exhaust stream (short circuit).

Mass and energy balances between the zones and flows to and from the cylinder allow computation of the perfect displacement zone's purity and the purity of the exhaust stream. The former will not be unity always because of some possible back flow from the cylinder to the transfer ducts. Such back flow was accounted for in the model. The percentages of the gas which flow into the perfect displacement zone and exhaust stream were assumed to vary linearly with the amount of gas which has flowed *via* the transfer port into the cylinder since that port opened. Constants for determining the relationship in this study were determined from experiments by Blair [3] and Corberan et al. [9].

2.4.3. The combustion model

A comprehensive combustion model would increase the computational effort for a full engine simulation unacceptably. Provided that only gross engine performance parameters are required, conventional wisdom (Corberan et al. [9], Chiou et al. [7]) suggests that a single zone model is adequate. Over each time interval the equation describing the combustion process is similar to Eq. (17) except that there is no flow into the cylinder during combustion, and there is also heat lost through the cylinder surfaces (q_l) and heat added by the combustion process (q_c) over each time interval. Thus

$$M^{j+1} = M^j$$

and

$$(ME)^{j+1} = (ME)^j + q_c - q_l - \tfrac{1}{2}\left(P^{j+1} + P^j\right)\left(V^{j+1} - V^j\right). \tag{19}$$

When the exhaust port shuts, the amount of fresh charge which has entered the cylinder during scavenging is known from accumulating mass fluxes through the transfer and exhaust ports at each stage of the cycle, and the purity of this gas is known from repeated application of Eq. (18) during scavenging. The mass of fuel in the combustion chamber can therefore be calculated from this and the trapped air/fuel ratio, which is an input to the model. Blair [3] has estimated that losses due

to imperfect combustion leave about 85–90% of this mass available for complete combustion. It is generally accepted [7,9] that the *fraction* of this mass burnt, is related to the crankshaft angle (ϕ) by the Weibe function

$$M_{\text{burnt}} = 1.0 - \exp\left[-y_a\left(\frac{\phi - \phi_c}{\phi_b}\right)^{y_e+1}\right], \quad \phi_c \leqslant \phi \leqslant \phi_c + \phi_b, \tag{20}$$

where y_a and y_e are experimentally determined values which are set at 8.0 and 1.0, respectively, in this study, ϕ_b is the total number of degrees of crankshaft revolution over which combustion takes place and ϕ_c is the crankshaft angle at the onset of combustion. For spark ignition engines, ϕ_b lies between 50° and 60° and ϕ_c corresponds to a crankshaft angle of about 10° before the piston reaches the top of its stroke. The heat added between crankshaft angles ϕ^j and ϕ^{j+1} corresponding to the beginning and the end of a time interval is therefore

$$q_c = C_{\text{val}} \int_{\phi^j}^{\phi^{j+1}} \mathrm{d}M_{\text{burnt}},$$

where C_{val} is the fuel calorific value.

A number of correlations exists for q_l, the heat lost through the combustion chamber walls. The one used in this study was developed by Rassweiler and Withrow [19], and allows the losses to be expressed in terms of the cylinder volumes and pressures at the beginning and end of the time interval. This and the calculation of q_c allows the cylinder state at the end of each time interval during combustion to be calculated by solving Eq. (19) using successive substitution.

Engine output was not terribly sensitive to the actual Weibe function parameters, but varied considerably with trapped air/fuel ratio, combustion efficiency and crank angle at ignition.

During the period when the cylinder was closed, and no combustion was taking place, a polytropic relationship was used to calculate air states. The indices used were 1.25 for compression and 1.35 for expansion after Blair [3].

2.5. *Relationships between port areas and piston position*

Simple geometry provides a relationship between piston position and crankshaft angle. Piston and rotary ports were divided into up to ten slices of equal widths and a table of cumulative area as a function of crank angle was constructed for each port. During simulation, the piston position was used to interpolate these tables and to calculate the instantaneous port areas.

Reed ports were modelled using the instantaneous pressure difference across the port to drive a dynamic model of the vibrating reed petal. The theory is described in Hinds and Blair [13]. Calculations were terminated after the third mode of vibration.

3. Numerical results—standard problems

The numerical embodiment of the theory presented above was applied to modelling steady isentropic flow in a venturi, 1m in length, of minimum diameter 38mm and entering and leaving diameters 50mm. The constriction was located in the middle of the venturi. Figs. 2(a) and 2(b) show the pressure and

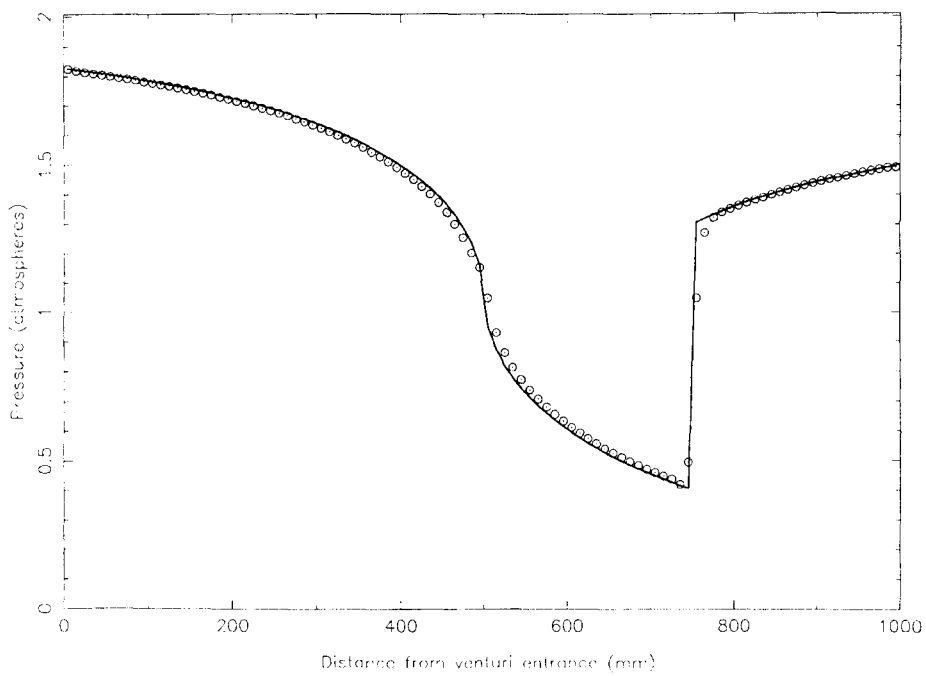

(a)

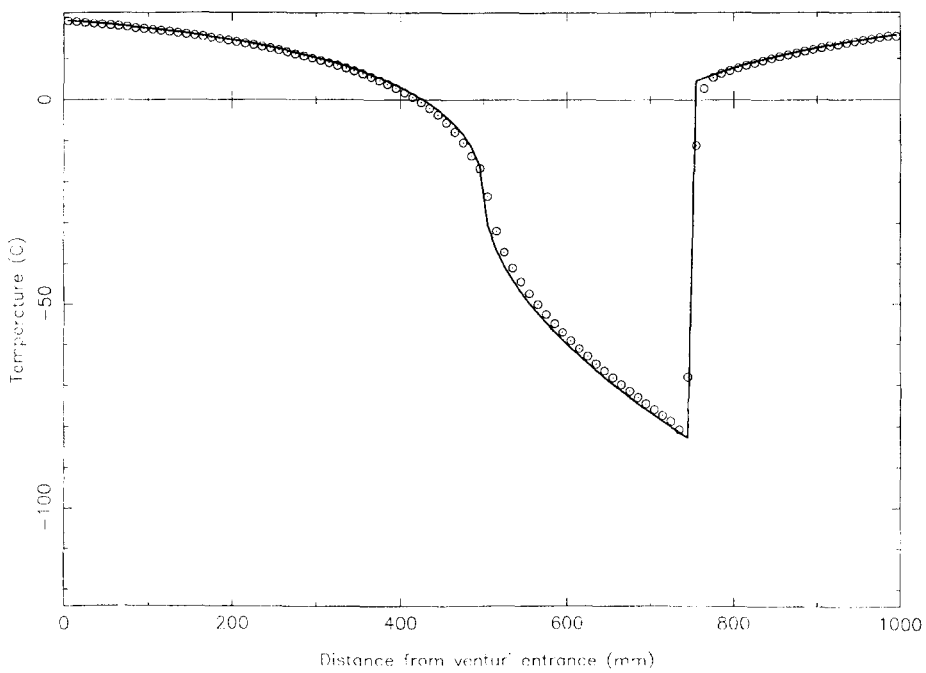

(b)

Fig. 2. (a) Variation of pressure in venturi. (b) Variation of temperature in venturi. $r = 1.33$, mesh = 10mm, —: analytical, ○: numerical.

temperature distributions, respectively, in the venturi for a Courant number of 0.8, a 10mm duct discretization, and the flux limiting parameter, $l = 0.55$. Numerical experiments show that when the duct discretization is increased to 20mm and $l \geqslant 0.75$, significant oscillations in the temperature distribution downstream of the shock occur. Much lower amplitude oscillations are evident in the pressure distribution. These oscillations are not evident at a 10mm discretization. For $l \leqslant 0.4$, there is significant diffusion present at the leading edge of the shock. Regardless of mesh size, the shock width appears to be about $2\frac{1}{2}$ mesh lengths. The difference between the numerical and exact solutions is three times as large as in Fig. 2 when a 20mm mesh size is used. However, the shock is always in the correct position regardless of mesh size, and the passage through extreme points is modelled well. There is no discernible difference between numerical solutions obtained for Courant numbers between 0.1 and 0.9. The good agreement between the numerical and experimental results at the venturi end points shows the effectiveness of the boundary condition model.

Qualitatively, the results are as good as or better than many of those described in the studies of Yang and Przekwas [25] which compared the performance of a number of TVD, ENO (essentially non-oscillatory), FCT (flux corrected transport) and Riemann solver based schemes applied to the 1D Burger's equation. Several of those schemes produced oscillations near wave fronts and others were highly diffusive, unlike the scheme discussed herein.

The results are not as good as those obtained by Corberan et al. [8], who based their second order TVD scheme on the work of Roe [20] and Harten [12]. There appears to be negligible difference between their solution and the analytical one for a 20mm duct discretization of the above venturi problem, the shock width being only one mesh length. However, the algorithm involves considerably more computation than the one described in this study, and requires special additions to avoid entropy violating shocks. As mentioned earlier, the numerical scheme in this study is able to select the correct (entropy satisfying) solution.

When compared with a numerical solution to the contact discontinuity problem using a flux corrected transport (FCT) scheme (Winterbone and Pearson [24]), the scheme described in this study exhibited no oscillations whereas the FCT scheme showed some oscillations on wave peaks immediately behind the start of a contact discontinuity.

4. Numerical results—engines

Engines are simulated by running them numerically for a number of revolutions and calculating all duct and box states at each time step. Time steps vary with crank angle and duct spatial discretization, but correspond typically to less than one degree of crankshaft revolution. Each simulation continues until steady power outputs are obtained on successive revolutions. High performance two-stroke engines have exhaust duct profiles similar to those shown in Fig. 1. The largest diameter may be of order 100mm whilst the smallest may be of order 20mm. The change between these two extreme diameters can take place over a length of less than 50mm. Numerical experiments show that to obtain results which exhibit little variation with mesh size, such ducts require spatial discretizations between 10mm and 20mm, depending on the rapidity of duct cross-section area change. Clearly, larger mesh sizes could be used in ducts of less variable cross-sections. For ducts like those in Fig. 1, a variable discretization could be used to cater for regions of rapid cross-section area change. As shown in Fig. 3, there was little variation in power between simulations using 10mm meshes and those using smaller

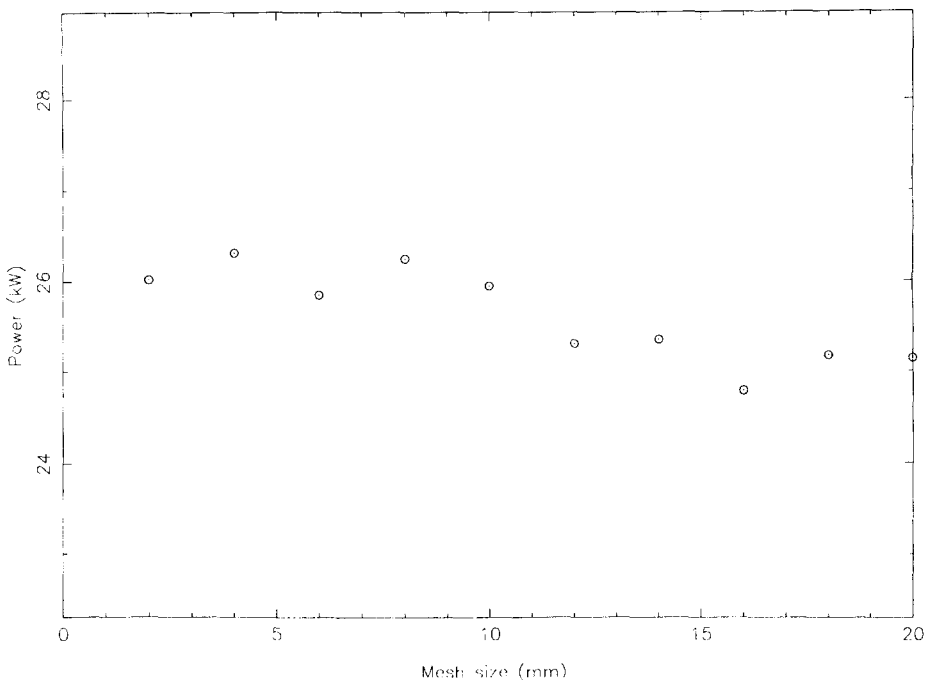

Fig. 3. Variation of power with mesh size.

ones in the simulation of a 125cc Rotax model R128 engine operating at 12000 rpm. Similar results were obtained for other engines over their operating speeds. As 10mm meshes give rise to typically 100 cells in an exhaust duct, and a combined total of 30 cells in the remaining ducts, variable mesh length within a duct was not implemented in this study. 10mm meshes were therefore used in the remaining simulations.

Fig. 4 shows little variation of power output with Courant number for the Rotax engine running at 12000 rpm. This and other numerical experiments led to a Courant number of 0.8 being used in the remaining simulations.

In Fig. 5, the difference in convergence behaviour with respect to numerical revolutions of the Rotax engine running at 12000 rpm and a reed valve induction Yamaha 80cc model B85 engine running at 13000 rpm is demonstrated. The Yamaha engine simulation converges in a much more oscillatory fashion than does the Rotax engine simulation. In general, reed valve induction engine simulations tend to converge in an oscillatory fashion whereas rotary valve and piston port induction engine simulations tend to behave like the Rotax simulation in Fig. 5. This convergence behaviour highlights the danger of terminating the simulations too early. The termination criterion used related to relative power differences over successive numerical revolutions being lower than some arbitrarily small number, usually 10^{-4}. A check was also made that over the last numerical revolution, the relative differences between gas masses entering and leaving each duct is smaller than 10^{-4}, thus ensuring mass flux conservation in each duct and in each engine box.

The remainder of the curves show the convergence behaviour of engine mass balance, and expansion chamber mass balance. Engine mass balance refers to the relative difference in the amounts of gas

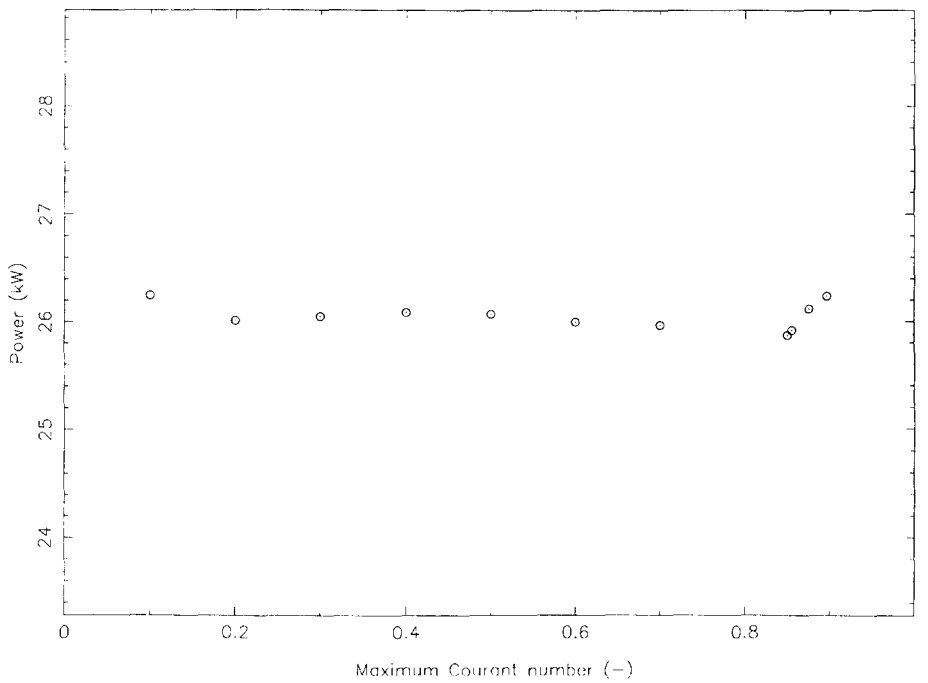

Fig. 4. Variation of power with Courant number.

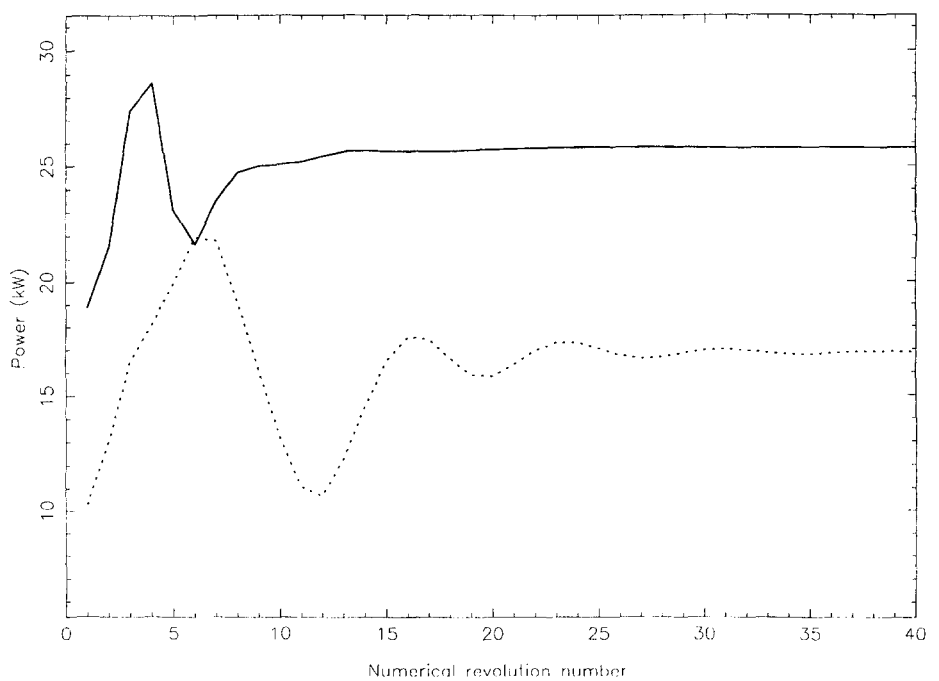

Fig. 5. Convergence of power with revolution number: solid/dotted line = rotary/reed valve engines.

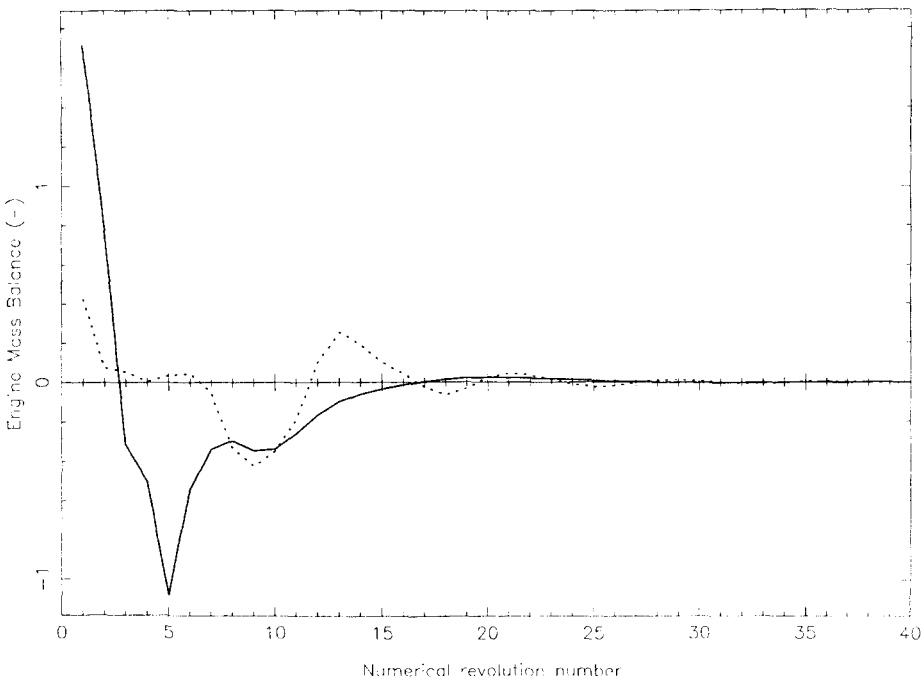

Fig. 6. Convergence of engine mass balance: solid/dotted line = rotary/reed valve engines.

entering the inlet port and leaving the exhaust port over an engine revolution. Duct mass balance refers to the relative difference in the amounts of gas entering the exhaust duct and leaving it over an engine revolution. The mass balance convergence behaviour in Fig. 6 for both engine simulations mirrors the corresponding power convergence behaviour, albeit at lower relative amplitudes of oscillation. Figs. 7(a) and 7(b) show the corresponding duct mass balances. Fig. 7(b) shows that these balances for both engines can be made to decrease to arbitrarily small values by increasing the number of numerical revolutions simulated. This is to be expected, given that a flux conservative numerical method has been used to model duct flows.

To obtain engine and duct mass balances as low as 10^{-6}, it is often necessary to run the simulation for over 50 revolutions. By this time, the power is usually changing from revolution to revolution by less than 0.01%. Forty seven numerical revolutions of the Rotax engine at 12000 rpm took 145 CPU seconds on a 166MHz Pentium computer. The variation in CPU time is approximately linear with engine speed and approximately quadratic with the duct discretization, indicating that most of the CPU time is spent in the duct flow modelling routine. Tests show that approximately 10–15% of the simulation time is spent in boundary condition computation. Simulation studies with the model show that arbitrarily small energy balances between fluid inflow/outflow for each duct can also be obtained if the friction factor is set to zero. The value used in the results presented here was 0.004. Comparable momentum balances can be achieved for zero friction factor and constant duct cross-section. Energy and momentum balances need to be conducted on the entire duct (not just the fluid inflow/outflow) when these two effects are present. In such cases, the overall balances are still less than 10^{-5}.

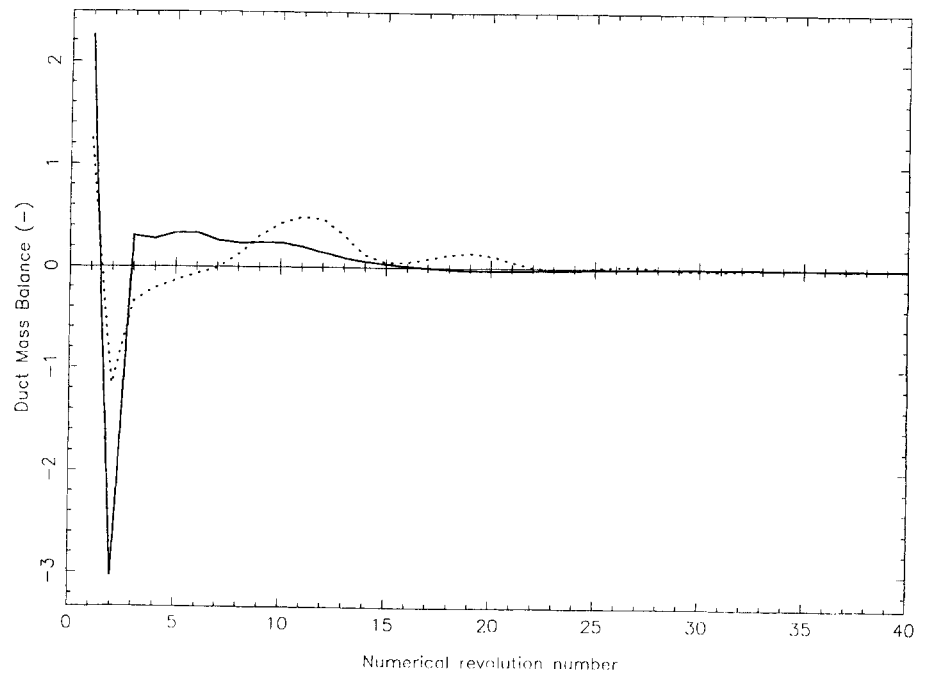

(a)

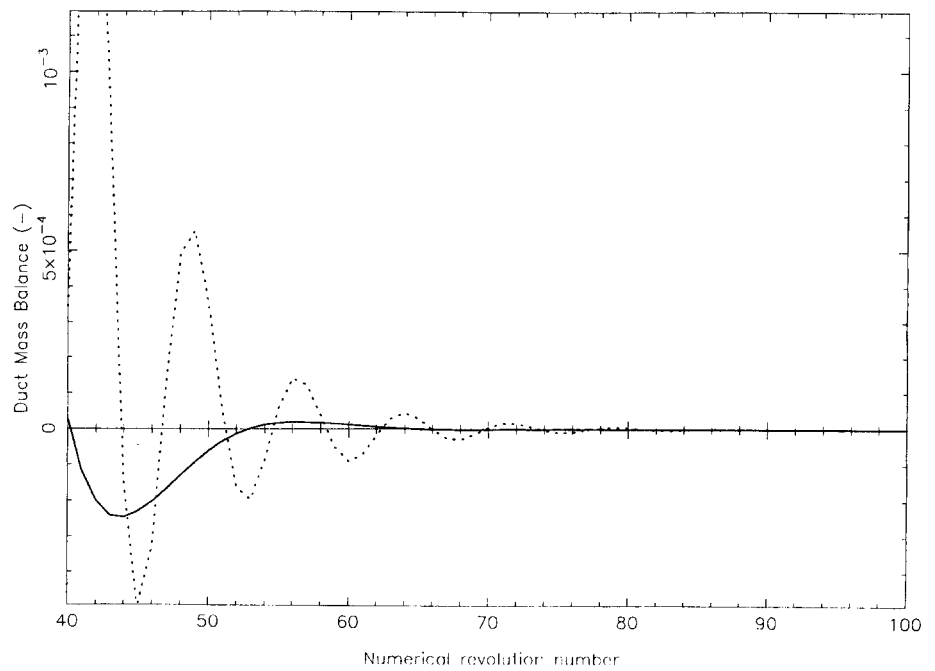

(b)

Fig. 7. (a) Convergence of duct mass balance. (b) Convergence of pipe mass balance. Solid/dotted line = rotary/reed valve engines.

Pairs of simulations run using values of the flux limiter parameter, l, between 0.5 and 1.0 produced power variations of less than 1% in the many cases tested. In animations of the exhaust duct temperature and pressure waves, no oscillations in either variable was evident for the many values of the limiter tested, in contrast to the results for the venturi in Section 3. However, all remaining numerical experiments described herein were carried out with $l = 0.55$.

The simulation has been tested on a large number of engine configurations and has, in 99% of cases, converged to a steady power output. Corberan et al. [9] and Blair [3] noted that sometimes a periodic variation in output of relatively high amplitude occurred which no amount of numerical revolutions seemed to cure. These occurred in early studies with this model and were found to be due to one or more of the following:

- A mismatch in the relative mesh sizes in the hot and cold ducts, hence the actions relating to this taken in Section 2.2.5.
- Inaccurate modelling of flow reversals at ports. Considerable time was spent constructing a robust port boundary condition calculator which was very sensitive to flow direction reversals.
- Insufficient damping in the reed valve models. A totally undamped model often produced almost random fluctuations in power from revolution to revolution unlike the periodic variations which Corberan et al. [9] suggested might be due to problems with their reed petal vibration model. Their model appears to be almost identical to the one used in this study. The minimum amount of damping to stabilize the convergence was added to each mode of vibration in the study described herein. The slow convergence of the B85 engine shown in Figs. 5–7 could well be due to its reed induction system; the important point being that it does converge to arbitrary precision eventually.

In the 1% of cases that did not converge, periodic fluctuations in power with numerical revolution of less than 0.5% occurred. These were eradicated dynamically by sensing the oscillations and reducing (by about 5%) the maximum allowable Courant number.

5. Experimental results

Figs. 8 and 9 show comparisons between simulated and experimental results for a Parilla 100cc model T75 engine and the Rotax engine mentioned above.

The experimental results for the Parilla were obtained from an eddy current dynamometer with a high quality load control system. A key feature of the results is that the model predicts the position and magnitude of the peak power, indicating that the wave speed modelling mechanism is very good. From the results taken during a number of different runs made under the same conditions, the dynamometer appeared to have an error of less than about 8%. Apart from experimental error, the discrepancies between experiment and model predictions away from the position of peak power could well be due to uncertainties in the following parameters used in the model:

- the Weibe function parameters (Section 2.4.3),
- the scavenging parameters (Section 2.4.2),
- the combustion efficiency,
- the air-fuel ratio,
- the assumed discharge coefficients (Section 2.3.1),

all but the last of which vary to some extent with engine speed. Considering that mean estimated values for these were taken from the literature, and no attempt was made to "tune" these values to

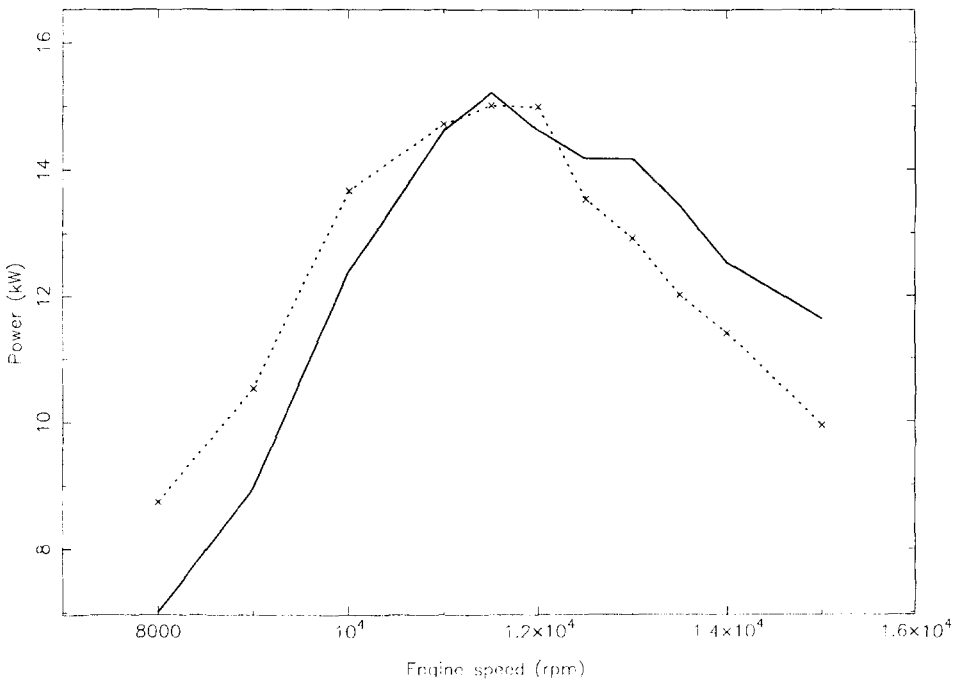

Fig. 8. Simulated and experimental results for the Parilla engine. Crosses: simulated, solid line: experiment.

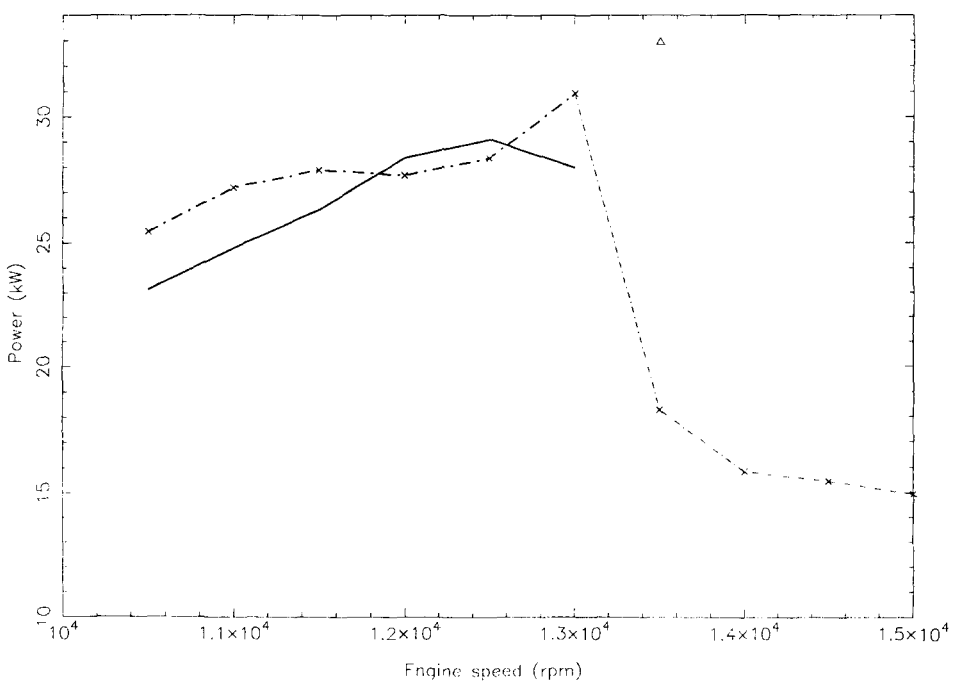

Fig. 9. Simulated and experimental results for the Rotax engine. Crosses and triangle: simulated, solid line: experiment.

match the experimental results, the agreement between the latter and the results predicted by the model is quite good.

Raw experimental data for the Rotax engine were collected from a track-side data acquisition system monitoring sensors in a go-kart, and processed to provide the results shown. The need for drivers to keep the engine in its power band reflects the narrow range of engine speeds over which the data are available. Given that the errors which can occur in this type of testing are quite high, the simulated and experimental results are in good agreement. Possible sources of error are the same as those stated above for the Parilla engine, plus additional ones related to the inherent errors in an indirect data acquisition system of this type.

An engine simulation needs to be started with all state variables initialized in all boxes and ducts. The final convergence should be independent of these initialized states. Tests showed that this was not the case for the Rotax engine in this study, and other engines of similar specific power output. The effect can be seen in Fig. 9, where the triangular point was obtained by starting the simulation at 13500 rpm using the duct and box states attained after converging the simulation at 13000 rpm. On the other hand, the cross at 13000 rpm was obtained by starting the simulation at that speed using low temperatures and pressures for the initial box and duct states. Exhaustive tests showed that:

- There seem to be two solutions which exist only over a narrow speed range, close to the peak engine power and at speeds beyond it.
- Only high specific power output engines exhibit this behaviour. For example, it proved impossible to obtain more than one solution for the Parilla engine at any speed.
- Points like that represented by the triangle in Fig. 9 were not obtained if the simulation was commenced at a high speed (for example, 15000 rpm for the Rotax engine) and subsequent simulations were at lower speeds with no duct and box state variable re-initialization.
- Curves similar to that represented by the crosses in Fig. 9 appear to match experimental results, although some go-kart drivers have reported inconsistent power surges beyond the generally accepted engine power band. This second solution may explain these surges. Careful testing with a dynamometer may be able to resolve this problem.
- Spoiling the scavenging characteristics in the dual solution region removes the upper solution.
- Both solutions show that the power drops very sharply from its peak, in agreement with the simulation results shown by Corberan et al. [9] who modelled duct flows using a totally different TVD method than that used in this study.

The tempting explanation that one of the two solutions is physically unreasonable is somewhat nullified by the fact that the flux splitting algorithm is supposed to produce only physically reasonable solutions (Yang and Przekwas [25]). The flux limiting procedures and conservative Courant numbers (0.8) adopted in this study decrease the likelihood of an entropy decreasing solution occurring. These statements can be proven for linearized equations only, so there is only a very small chance that one of the solutions is physically unreasonable. However, despite exhaustive tests, no numerical evidence was found for this conjecture. The matter is being investigated further.

Apart from the above considerations, the match between experimental and simulated results for the Rotax engine is quite reasonable, given the possible errors in the experimental equipment. Much more accurate data needs to be acquired, over larger engine speed ranges before the model parameters can be tuned further.

6. Conclusions

The conclusions from this study can be summarized as follows:

- The comprehensive simulation model of the two-stroke engine demonstrates good numerical convergence to its solutions and conserves mass, momentum and energy to arbitrary precision in each engine duct, and through the chambers of the engine itself.
- Simulations of reed induction engines appear to take longer to converge than those of rotary valve and piston ported engines.
- The model sometimes predicts two different power curves in a small region above the engine speed giving peak power, depending on the initial states of box and duct variables. Although there is a small body of evidence to suggest that both these solutions may exist, this needs much closer examination.
- Apart from the last point, good agreement between simulated and experimental results was obtained for two engines of widely differing performances.

Acknowledgements

The author gratefully acknowledges the assistance given by his colleague Malcolm Littler in the form of helpful suggestions and development of a user friendly front end to drive the model. He is also indebted to Ian Williams of Ian Williams Tuning for providing experimental data.

Appendix A

A.1. Nomenclature

A	cross-section area of duct or port (m^2).
a	local speed of sound in gas (ms^{-1}).
$\tilde{a}$	"pseudo" local speed of sound (see Eq. (10)) (ms^{-1}).
c_p	specific heat at constant pressure ($Jkg^{-1}K^{-1}$).
c_v	specific heat at constant volume ($Jkg^{-1}K^{-1}$).
D	diameter (m).
E	internal energy per unit mass (Jkg^{-1}).
$E_0(E+U^2/2)$	stagnation internal energy (Jkg^{-1}).
f	friction factor (–).
$F_\rho\ (\rho U)$	mass flux ($kgm^{-2}s^{-1}$).
$F_\xi(\rho U^2+P)$	momentum flux ($kgm^{-1}s^{-2}$).
$F_\zeta((\rho E_0+P)U)$	stagnation internal energy flux ($Jm^{-2}s^{-1}$).
$G(4fu\|u\|/(2D))$	friction contribution to momentum equation (ms^{-2}).
$H(E+P/\rho)$	enthalpy per unit mass (Jkg^{-1}).
$H_0(H+U^2/2)$	stagnation enthalpy (Jkg^{-1}).
l	flux limiter variable (Section 2.2.3) (–).
M	mass of fluid in box (kg).

m	mass of fluid in duct (kg).
P	local (superposition) pressure (Pa).
Q	one of ρ, ξ, ζ, P.
$\dot{q}$	heat transfer rate per unit mass of fluid (Wkg^{-1}).
R	gas constant for given gas ($\mathrm{Jkg}^{-1}\mathrm{K}^{-1}$).
r	pressure ratio across venturi tube (–).
T	temperature (K).
U	particle velocity (m/s).
V	box volume (m^3).
v	cell volume (m^3).
W	box purity (kg air/kg gas).
w	duct gas purity (kg air/kg gas).
x	spatial co-ordinate (m).
$\tilde{Z}$	flux-split matrix (see Eq. (6)).

A.2. *Greek symbols*

δx	spatial discretization step (m).
$\delta\theta$	time discretization step (s).
$\gamma(c_\mathrm{p}/c_\mathrm{v})$	ratio of gas specific heats (–).
$\tilde{\gamma}$	"pseudo" specific heat ratio (see Eq. (7)) (–).
λ	elements of $\tilde{\Lambda}$ (ms^{-1}).
$\tilde{\Lambda}$	matrix of eigenvalues of $\tilde{Z}$.
ρ	gas density ($\mathrm{kg\,m}^{-3}$).
θ	time (s).
ϕ	Crankshaft angle with datum at the top of the piston stroke (degrees/radians).
$\xi(\rho U)$	momentum ($\mathrm{kg\,m}^{-2}\,\mathrm{s}^{-1}$).
$\zeta(\rho E_0)$	stagnation internal energy per unit volume (Jm^{-3}).

A.3. *Subscripts*

amb	calculated at ambient air states.
i	cell number.
stag	calculated at fluid stagnation states.
wall	calculated at wall states.

References

[1] W.J.D. Annand and G.E. Roe, *Gas Flow in the Internal Combustion Engine* (G.T. Foulis & Co., Sparkford, Somerset, Yeovil, UK, 1974).

[2] R.S. Benson, R.D. Garg and D. Woollatt, A numerical solution of unsteady flow problems, *Internat. J. Mech. Sci.* 6 (1964) 117.

[3] G.P. Blair, *The Basic Design of Two Stroke Engines*, SAE Book R 104 (1990).

[4] G.P. Blair, An alternative method for the prediction of unsteady gas flow through the internal combustion engine, SAE Technical Paper No. 91-1850 (1991).
[5] G.P. Blair and W.L. Cahoon, A more complete analysis of unsteady gas flow through a high-specific-output two-cycle engine, SAE Technical Paper No. 72-0156 (1972).
[6] G.P. Blair, H.B. Lau, A. Cartwright, B.D. Raghunathan and D.O. Mackey, Coefficients of discharge at the apertures of engines, SAE Paper No. 95-2138 (1995).
[7] J.S. Chiou, M.S. Chiang and C.K. Chen, Numerical simulation method applied to the multi-expansion exhaust system in a two-stroke engine, *J. Automobile Engrg.* (1995) 281–288.
[8] J.M. Corberan and M.Ll. Gascon, TVD schemes for the calculation of flow in pipes of variable cross-section, *Math. Comput. Modelling* 21 (3) (1995) 85–92.
[9] J.M. Corberan, R. Royo, A. Perez and J. Santiago, Optimization of a 125cc racing two-stroke engine based on modelling and testing, SAE Paper No. 94-2516 (1994).
[10] S.F. Davis, TVD difference schemes and artificial viscosity, ICASE Report No. 84-20 (1984).
[11] B. Grossman and R.W. Walters, An analysis of flux-split algorithms for Euler's equations with real gases, AIAA Paper No. 87-1117 (1987) 177–187.
[12] A. Harten, On a class of high resolution total-variation-stable finite-difference schemes, *SIAM J. Numer. Anal.* 21 (1984) 1–23.
[13] E.T. Hinds and G.P. Blair, Unsteady gas flow through Reed valve induction systems, SAE Paper No. 78-0766; presented at the Off Highway Vehicle Meeting and Exposition, Milwaukee (1978).
[14] J.D. Hoffman, *Numerical Methods for Scientists and Engineers* (McGraw-Hill, New York, 1990).
[15] J.H. Keenan and J. Kaye, *Gas Tables* (Wiley, New York, 1948).
[16] T. Neumeyer, G. Engl and P. Rentrop, Numerical benchmark for the charge cycle in a combustion engine, *Appl. Numer. Math.* 18 (1995) 293–305.
[17] M. Poloni, D.E. Winterbone and J.R. Nichols, Comparison of unsteady flow calculations in a pipe by the method of characteristics and the two-step differential Lax–Wendroff method, *Internat. J. Mech. Sci.* 29 (5) (1987) 367–378.
[18] W.H. Press, W.T. Vetterling, S.A. Teukolsky and B.P. Flannery, *Numerical Recipes* (Cambridge University Press, Cambridge, 2nd ed., 1992).
[19] G.M. Rassweiler and L. Withrow, Motion pictures of engine flames correlated with pressure cards, *SAE J.* 42 (1938) 185; Reissued as SAE Paper No. 80-0131 (1980).
[20] P.L. Roe, Approximate Riemann solvers, parameter vectors and difference schemes, *J. Comput. Phys.* 43 (1981) 357–372.
[21] J.L. Steger and R.F.J. Warming, Flux vector splitting of the inviscid gas-dynamic equations with applications to finite difference methods, *J. Comput. Phys.* 40 (1981) 263–293.
[22] B. van Leer, Towards the ultimate conservative difference scheme, V. A second order sequel to Godunov's method, *J. Comput. Phys.* 32 (1979) 101–136.
[23] F.J. Wallace and M.H. Nassif, Air flow in a naturally aspirated two-stroke engine, in: *Proc. I. Mech. Engrg.*, Vol. 1b (1953) 515.
[24] D.E. Winterbone and R.J. Pearson, A solution of the wave equations using real gases, *Internat. J. Mech. Sci.* 34 (12) (1992) 917–932.
[25] H.Q. Yang and A.J. Przekwas, A comparative study of advanced shock-capturing schemes applied to Burger's equation, *J. Comput. Phys.* 102 (1992) 139–159.